Chiral Surface Morphology of a Curved Platinum Crystal

THESIS

submitted in partial fulfillment of the
requirements for the degree of

MASTER OF SCIENCE
in
PHYSICS

Author :	Tycho Roorda
Student ID :	s1917781
Supervisor :	Tjerk Oosterkamp
2nd corrector :	Ludo Juurlink

Leiden, The Netherlands, March 31, 2020

Chiral Surface Morphology of a Curved Platinum Crystal

Tycho Roorda

Huygens-Kamerlingh Onnes Laboratory, Leiden University
P.O. Box 9500, 2300 RA Leiden, The Netherlands

March 31, 2020

Abstract

The study of stepped surfaces is fundamental to the fields of catalysis, nanostructure and chemical surface bonding. In this thesis, we characterize the range of surface structures present in a curved platinum crystal, miscut such that the curvature is perpendicular to the $[11\bar{2}]$ direction. Surface preparations include argon sputtering and annealing cycles. Auger electron spectroscopy has been used to confirm the chemical composition at the surface and low energy electron diffraction has been used to determine the surface structure. Scanning tunneling microscopy was used to image the surface and study its terrace width distribution and step density. Vacancy islands were studied to determine the chirality of the surface. A short to long edge ratio of 0.65 ± 0.06 is found in vacancy islands. Quantifying defect sites shows a surplus of reactive sites on the surface where step density is lower than $0.005\ \text{nm}^{-1}$.

Contents

Version of March 31, 2020– Created March 31, 2020 - 09:26

Chapter 1

Introduction

Structure and bonding at step sites play an import role in catalysis, nanostructure growth and adsorption behaviors. In the last decade, spherical and cylindrical crystals have been studied increasingly for their range of vicinal surfaces on a single surface[1–3].

We provide scanning tunneling microscopic (STM) images which characterize the surface of a curved platinum crystal. With a curvature cut 31 degrees to the $[11\bar{2}]$ direction, the surface structure contains kinked step edges along the curvature. In this configuration, the kinks of the step edges are asymmetric on either side of the apex, resulting in a chiral surface. One of the goals for this crystal is to be able to adsorb chiral molecules to the surface for further experiments. For instance, limonene has been shown to have an enantiomeric shift in binding energy to a platinum $(532)^S$ surface[4].

Version of March 31, 2020– Created March 31, 2020 - 09:26

Chapter 2

Sample preparation

An 8x7 millimeter curved single crystal of platinum was prepared by spark erosion and sanding at Surface Preparation Lab in Zaandam, The Netherlands. The surface is cleaned by repeated cycles of argon sputtering and oxygen, hydrogen and vacuum annealing which has been optimized for this crystal. Auger electron spectroscopy (AES) and low energy electron diffraction (LEED) are used to examine the chemical cleanliness and surface structure of the crystal surface.

2.1 Experimental setup

All procedures are carried out in an OMICRON ultra high vacuum (UHV) chamber, named Jellyfish, as depicted in figure 2.1. This picture shows the analysis chamber, with behind it, the preparation chamber. In it are the AES, LEED, STM and storage wheel (for up to 8 other samples). Connected to the rear of the analysis chamber by a lock valve is the preparation chamber in which is found the sputter gun and connections for high voltage sample heating as well as a connection to the load lock. Sample displacement is operated via 3 different manipulator arms and a wobble stick for the STM. The entire setup is supported on 4 concrete slabs which are isolated from the main floor and have a dedicated vibration dampening system attached to the foundation of the building. At the right side of the image is the control tower for the vacuum pumps (3 turbo pumps, a rough pump and two ion pumps), electronic gate valves and sputter gun. Two other control towers host the controls for the sample heating, AES, LEED and STM operation.

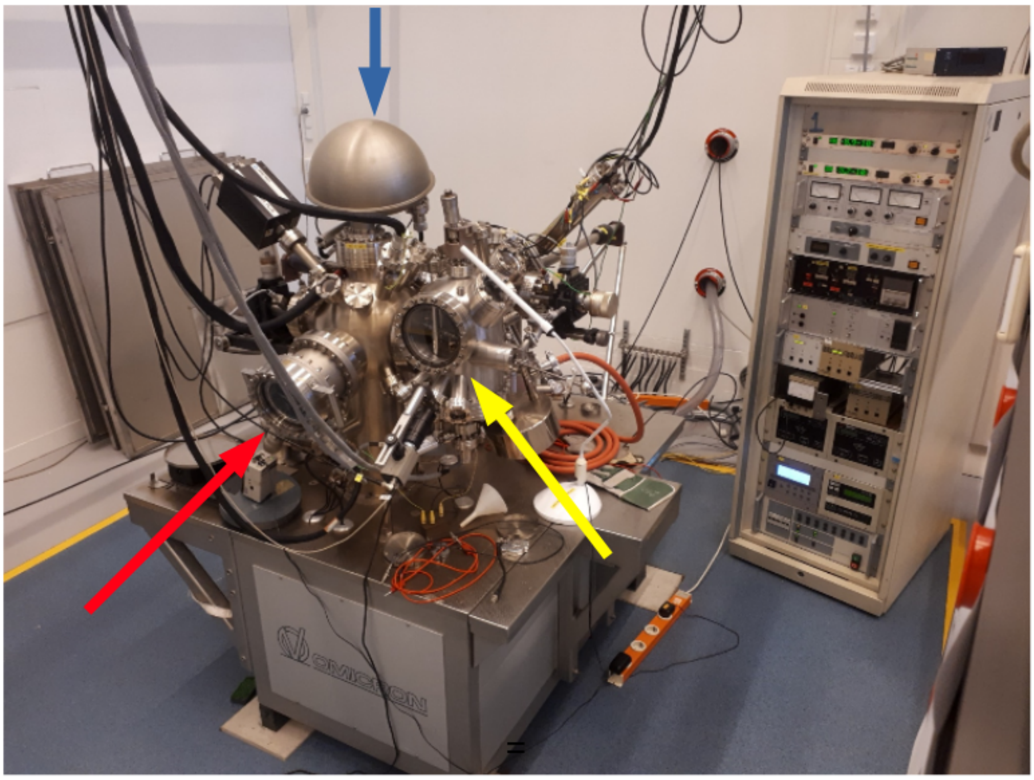

Figure 2.1: *Omicron STM setup showing AES (blue arrow), LEED (red arrow) and STM (yellow arrow) with control tower for pumps gauges and valves on isolated measurement island.*

2.2 Crystal surface structure

The apex of the crystal, located along the center, contains the (111) plane as shown in figure 2.2a. The curvature has a radius of 15 millimeter with a linearly increasing step density towards the edges, thus providing a large and continuous range of vicinal surfaces. By setting the curvature perpendicular to the $(11\bar{2})$ plane, or at an angle of 31 degrees to the [110] direction, the atomic steps along the curvature form kinked step edges. They consist of alternating sections of A and B step types separated by inner and outer kinks. The step edges on either side of the crystal form an asymmetry in their kinks which can be observed and used to adsorb chiral molecules to the surface.

Figure 2.2c shows a face centered cubic (FCC) {432} surface structure with kinked steps indicating the A and B type step edges. A-type step edges, indicated by blue spheres, can be identified by two neighbouring atoms at the step edge located above two other neighbouring atoms in the atomic layer below, as in the (100) surface. In contrast, two neighbouring atoms of B-type step edges, indicated by red spheres, are located above a single atom in the lower layer, as in the (110) surface. Alteration between A and B step types or B and A step types cause anti-symmetry. The chirality of the surface can be distinguished by (R) and (S) as decreasing order of atomic density of microfacets, so from {111} to {100} to {110}, as described in McFadden et. al.[5].

The terrace width, TW, can be determined from the angle, α, between the line normal to the surface and the terrace with the step height (or interatomic distance), $h = 0.226$ nm. Since α is dependent on the distance from the apex, we use the equivalent triangle as shown in figure 2.2b with x as the distance from the apex and $(R - \epsilon)$ as the base of the triangle. Since $R \gg \epsilon$, the base of the triangle can safely be approximated by $R = 15$ mm, the radius of curvature. From that, we obtain the following equation

$$TW = \frac{h}{tan\alpha} = \frac{h(R-\epsilon)}{x} \approx \frac{hR}{x} = \frac{0.226 \times 15 \times 10^6}{x} \tag{2.1}$$

which shows that the terrace widths are inversely proportional to the distance from the apex and so the step density, $\frac{1}{TW}$, increases linearly with

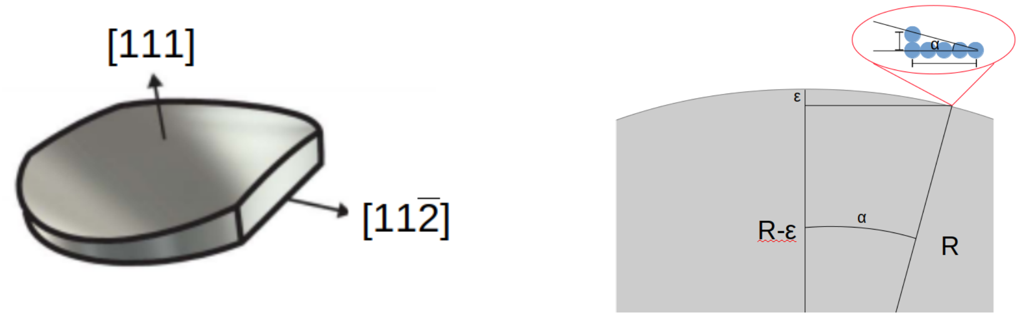

(a) *c-Pt(111)*

(b) *Depiction for TW calculation*

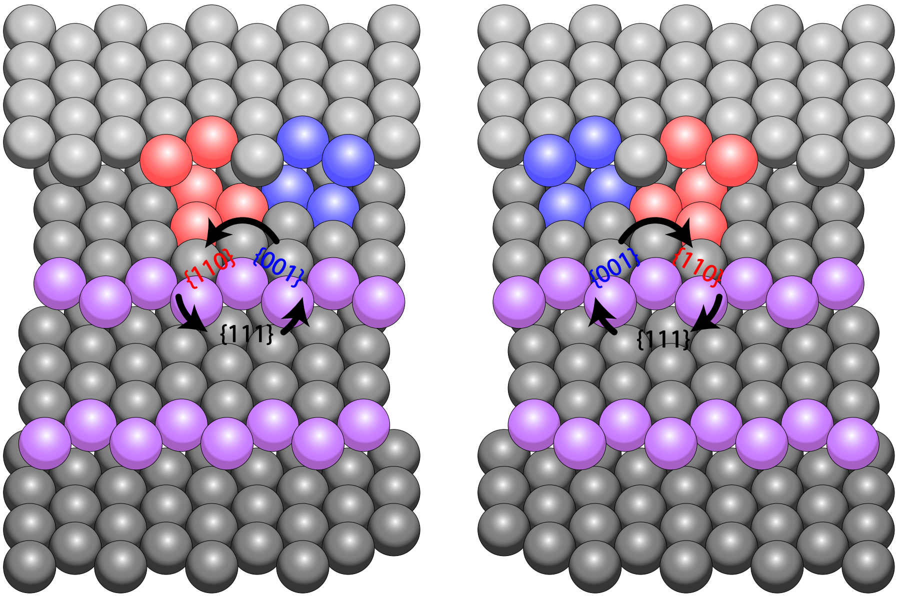

(c) *{432} Chiral surfaces*

Figure 2.2: *(a) Schematic drawing of our curved platinum crystal perpendicular to the (11$\bar{2}$) plane, 31 degrees to the (110) plane. Adapted from [2]. (b) Depiction of a TW calculation showing a magnified side view of terrace atoms with the equivalent triangle of the crystal. (c) Crystal structure of FCC {432} planes showing difference between A (blue spheres) and B (red spheres) type step edges with step atoms indicated by purple spheres. The chirality in the left and right images, indicated by the clockwise or counter clockwise rotation, represent the surfaces on opposing sides of the curvature. This figure has been made by S. Auras.*

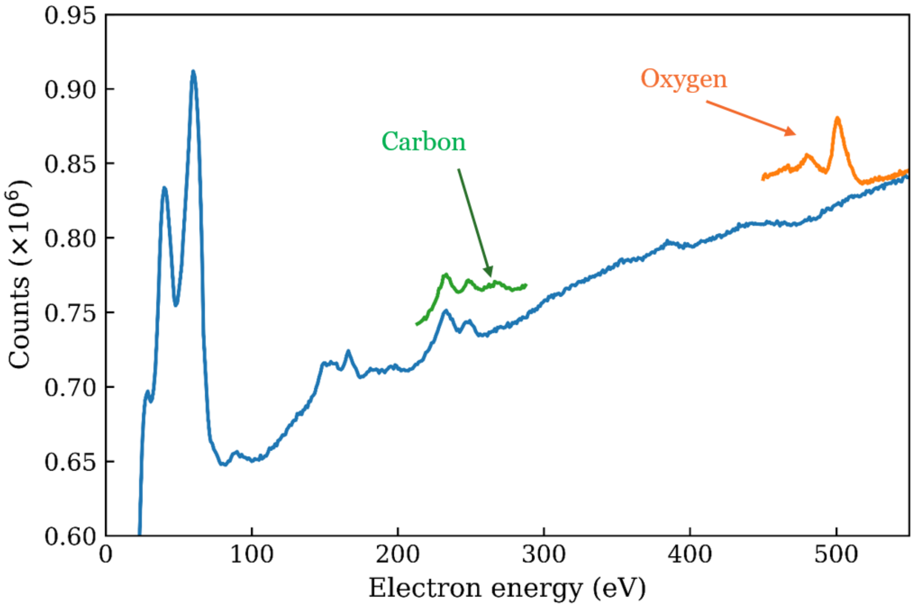

Figure 2.3: *Auger Electron Spectroscopy counts as a function of electron energy showing the spectrum of a clean platinum surface (blue curve). Green spectrum shows where carbon is expected at 272 eV and orange shows where oxygen is expected, near 500 eV.*

distance.

2.3 Auger electron spectroscopy

Auger electron spectroscopy (AES) is performed to test the chemical cleanliness of the crystal. A typical cleaning cycle consists of argon sputtering at room temperature and 0.52 keV for a duration of 10 minutes at 1.3×10^{-5} mbar followed by oxygen annealing at 3×10^{-8} mbar and 620 Celsius and finished with vacuum annealing at 920 Celsius. As a last cycle, to ensure proper surface reconstruction, argon sputtering is performed at an elevated temperature of 300 Celsius followed by vacuum annealing at 500 Celsius, each for 5 minutes.

Figure 2.3 shows Auger spectra for a clean platinum surface from 0 to

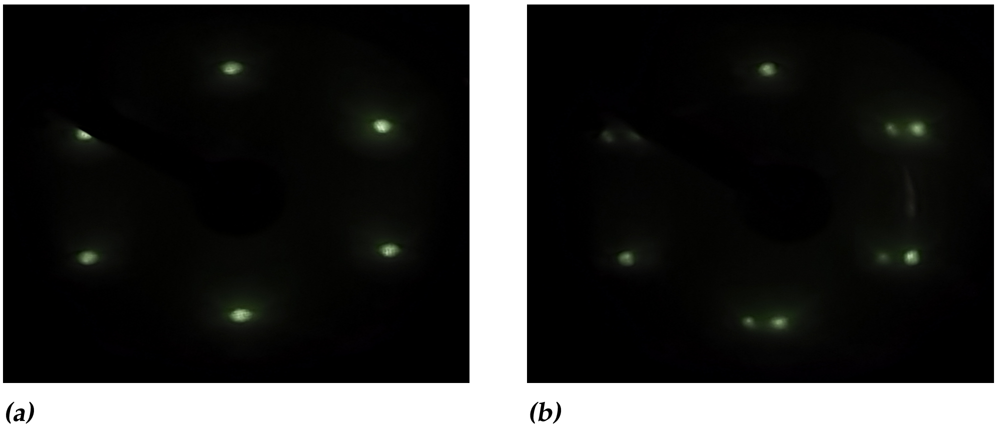
(a) **(b)**

Figure 2.4: *LEED images of (a) Pt(111) located at the center of the crystal and (b) 2.5 mm from the center, showing spot splitting at four LEED spots. Beam energy is 0.135 kV, filament is at 2.60 A.*

550 eV in blue as well as oxygen and carbon contamination peaks. The platinum spectra is recognized by the first group of major peaks at 56 and 64 eV with two smaller peaks at 43 and 93 eV. At the second set of peaks we find the expected 150, 158, 168, 185 and 199 eV followed shortly after by 217, 237 and 251 eV and finally some smaller peaks at 357 and 390 eV. More importantly is the absence of contaminants; carbon and oxygen peaks are shown in green and orange respectively at 272 eV and 454, 475, 490 and 510 eV. AES has been done on the crystal in three rows at 1 millimeter intervals along the curvature to ensure an overall, totally clean surface before proceeding. Some corners retained traces of oxygen. This was likely due to a non-circular focused beam which was reading traces of the frame holder.

If a high dose of oxygen is found at the surface then hydrogen annealing is used instead of oxygen annealing during a regular cycle. Sputtering for a duration of 60 minutes during a regular cycle is done when surface contaminants remain despite regular cleaning cycles. Over 40 cycles total were performed before the surface was clean and ready for STM.

2.4 Low Energy Electron Diffraction

The surface structure of the crystal is analysed by Low Energy Electron Diffraction (LEED). Figure 2.4 shows the LEED spots obtained while the electron beam is aimed at the center of the crystal (a) and 2.5 millimeters from the center (b). At the center of the crystal, we observe the face-centered cubic reciprocal spots of a FCC (111) surface where the center spot is hidden behind the electron beam. Along the curvature of the crystal, we observe spot splitting which increases proportionally with ratio of terrace width and step height. Figure 2.4b shows the clearest spot splitting observed near maximum spacing. In other words, the spot splitting is proportional to the step density, which follows a linear trend. Van Hove et. al.[6] provide a baseline of spot splitting to row spacing ratio expected at corresponding surface structure by Miller index. Comparing with data they provide will allow us to confirm proper surface structure.

LEED images were taken at quarter of a millimeter intervals along the curvature while maintaining surface to electron beam distance constant. Spacing between each spots is measured and averaged for each position. The spot splitting to row splitting ratio (SS/RS) as a function of deviation from the center is plotted in figure 2.5. The solid black lines are traced with a slope of 0.08165, based on results from van Hove et.al.[6]. In the center of the image there are no data points as the spots splitting distance can no longer be resolved. A good overlap with our data shows that step density increases linearly, as expected .

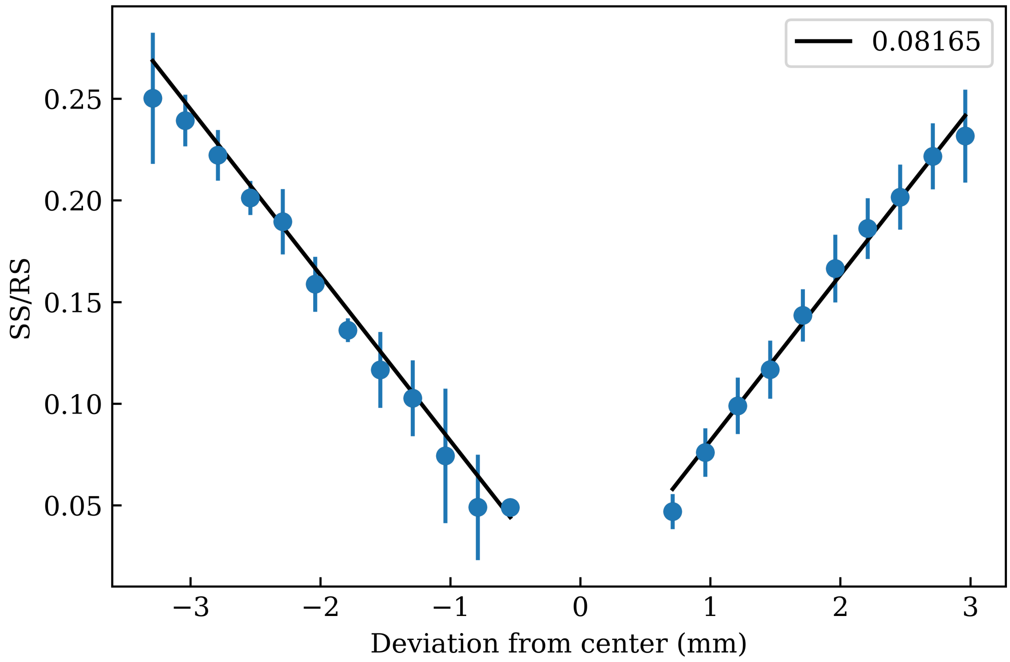

Figure 2.5: *LEED spot splitting to row spacing ratio as a function of deviation from the center. Data points are an average of the spot splitting points per position and error bars represent the standard deviation. Black solid line indicates expected slope from van Hove et. al. [6]*

Chapter 3

Scanning Tunneling Microscopy

Scanning tunneling microscopy was used to study, with near atomic resolution, the topography of the crystal surface. Over 1000 STM images were take along the curvature of the crystal. We observed single layer holes in wider terraces which could provide valuable insight in the surface structure. Additional images where taken at various locations to study the faceting of steps. These images however are not in the scope of this thesis.

3.1 Vacancy islands

Near the apex, larger terraces are expected. That is indeed observed, however they are often coated in vacancy islands (or holes), step bunching and occasionally local peaks. The cause of this is likely due to insufficient annealing which prevents the crystal from reaching thermal equilibrium in the larger terraces. Figure 3.1 shows a top view and bird's eye view of a local peak around 179 μm from the apex (+Y) and a local ridge. In (a), we clearly see 5 wide terraces ranging from a width of 200 to 600 nm and covered in 1 atomic layer deep holes. In the top left corner we can also observe a steep drop with heavy step bunching (hard to see with the color scale which is optimized to focus on the larger step surface). (b) shows the same surface but with a bird's eye view perspective. (c) shows a local peak with some bunching in between larger terraces and a few holes. (d) shows a local ridge where the middle terrace width is between 400 nm and up to over 1000 nm. On either side of the ridge, the surface steps down in opposite directions and all terraces are plagued with holes.

Noteworthy is that the formation of holes always takes the same shape

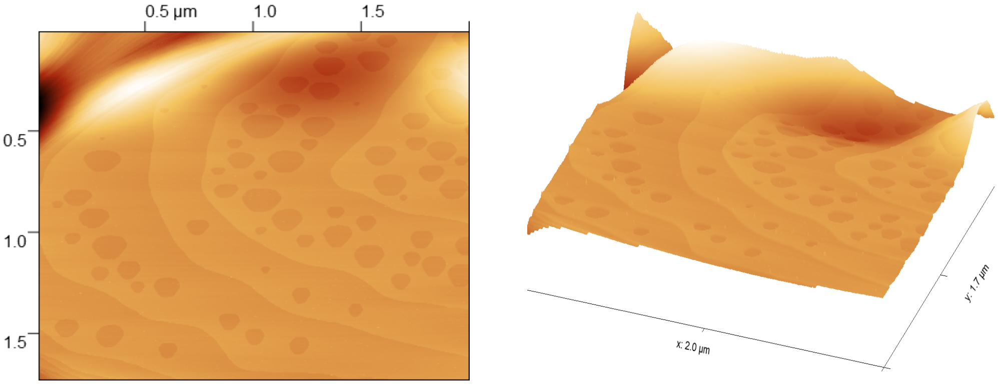

(a) Position: -171 μm **(b)** Bird's eye view of (a)

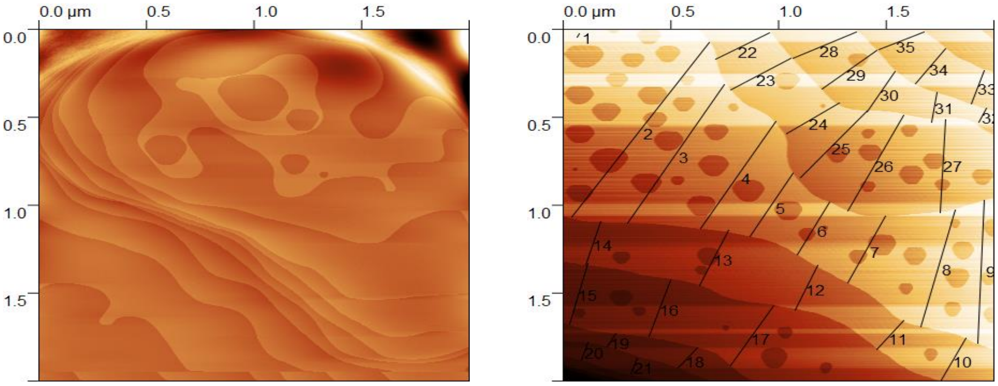

(c) pos: 0 **(d)** pos: 7.4 μm

Figure 3.1: (a) local peak with 200-600 nm wide terraces in a region of 20 nm wide expected terrace widths (b) bird's eye view of (a). (c) first selected apex (d) local ridge curving down towards both sides with an average terrace width of 375 nm and maximum of 1183 nm (indicated by line 2).

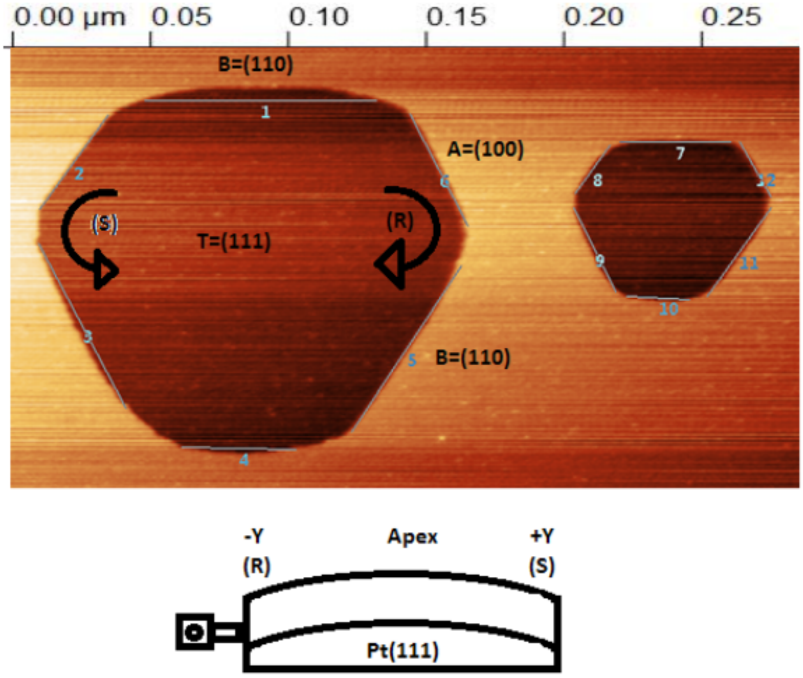

Figure 3.2: *Top: STM image of two large vacancy islands indicating which edges are predominantly A-type or B-type step edges and how the chirality is determined. Bottom: a schematic of the crystal with an eyelet referencing to the position in the sample holder to indicate chiral sides of the surface.*

and orientation. A vacancy island is formed from a total 6 sides of two different, alternating, lengths which correspond to A and B type step edges. The ratio between these edges is an equilibrium regulated by Wulff construction and line free energy, and is dependent upon annealing temperature [7]. The long edges can be identified as the energetically favorable close packed <110> direction (B-type) as determined by Lahee et. al. [8]. Therefore the short edges are of the <100> (A-type) direction. The ratio of the sum of A-type and B-type edges has been taken for 20 vacancy islands at 10 different locations near the apex. We find that the ratio of short to long edges is 0.65 ± 0.06 which overlaps perfectly with the findings of Michely et al.; 0.66 ± 0.05 [7].

Figure 3.2 shows two large vacancy island indicating where the A and B step edges are located as well as a sketch of our curved crystal as it is oriented in the sample holder. Following the schematic of figure 2.2c we can determine that the chirality in the vacancy islands is of (S) in the left hand corner and (R) in the right hand corner. Considering that holes step down in the opposite directions to which the crystal is curved, we can determine that the right side (+Y) of the crystal occupies (S) chirality and the left side (-Y) occupies the (S) chirality.

3.2 Terrace width distribution

Terrace widths have been accurately measured along 800 μm of the curvature at the apex. Figure 3.3 shows 4 different terrace distributions with lines indicating widths taken for their respective averages and maximums. In (a) we observe a single large terrace of over 1 μm next to a bunch of shorter steps with an average of 211 nm wide terraces located at -19 μm on the crystal, (b) shows more evenly distributed terrace widths at 1.6 μm on the crystal. We still observe a portion of bunched steps and some holes on the larger terrace. (c) and (d), located far enough from the apex, show much better terrace width distributions with averages of 8.7 and 8.4 nm.

Figure 3.4a shows the averaged terrace widths for each image, 300 μm on either side of the apex. Blue data with error bars represent each image's average terrace width and standard deviation. The red dots are, for each image, the local maximum terrace width which, together with the standard deviation, provide an idea of the terrace width distribution across the crystal. The black traced lines are the expected terrace widths as described by equation 2.1. We observe a close match with the expected ter-

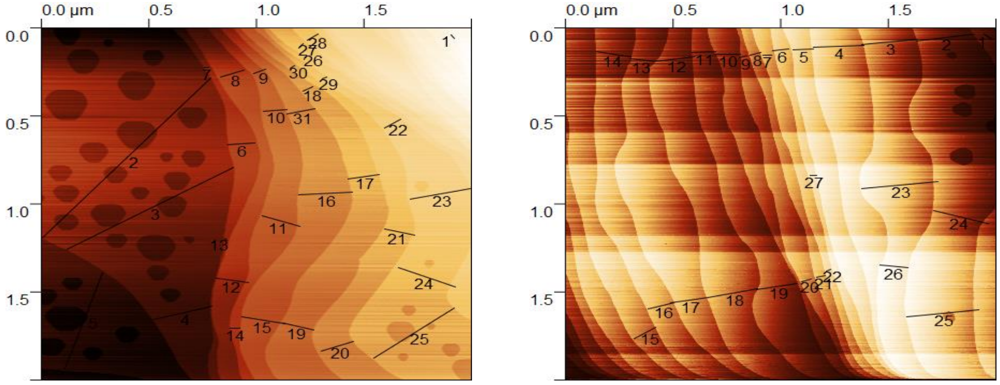

(a) *position: -19 µm* **(b)** *pos.: 1.6 µm*

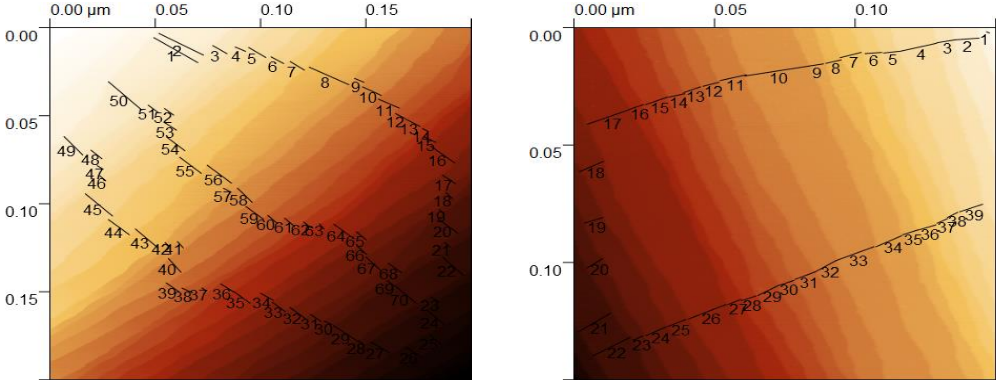

(c) *pos.: 117 µm* **(d)** *pos.: 385 µm*

Figure 3.3: *STM images showing line selection for terrace width distribution. (a) avg: 211 nm, max: 1200 nm (b) avg: 148 nm, max: 357 nm (c) avg: 8.7 nm, max: 24 nm (d) avg: 8.4 nm, max: 22 nm.*

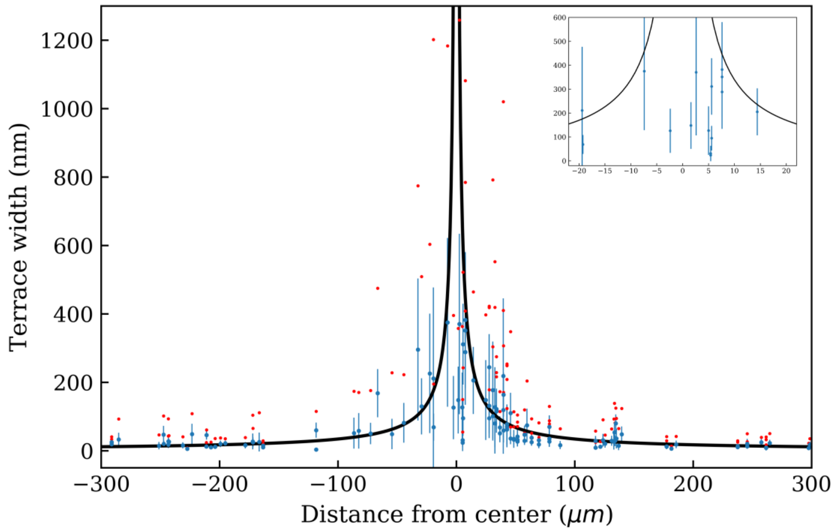

(a) *Terrace widths as a function of distance from the apex for 330 nm on either side of the apex. Blue data points indicate the average terrace widths including the standard deviation per STM image and red data points are the maximum terrace widths per image. A subfigure in the rop right shows a zoom around the center of the graph where the averages start to deviate from the expected TW curve (in black).*

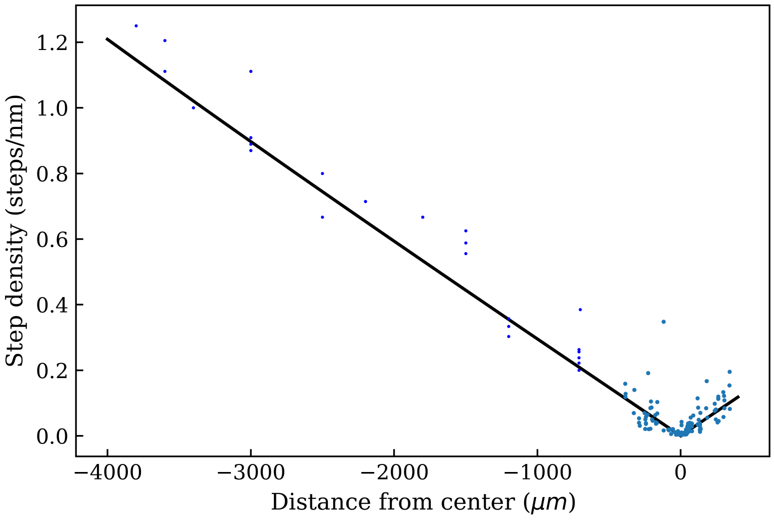

(b) *Step densities as a function of position on the crystal. With the same data as in (a) and further towards one edge of the crystal.*

race width except for in the ∼40 μm around the apex. This discrepancy is due to increased step bunching and hole formation where terrace widths reach above ∼300 μm.

By taking the inverse of the terrace widths, we expect to see a linearly increasing step density where the slope is determined by the radius of curvature and interatomic distance. Beyond 400 μm on the (-Y) side of the crystal, step densities were taken from STM images. In this region, terrace width distribution was low enough to simply divide the number of steps in an image by the distance between the first and last step. This data, along with the inverse of the terrace widths previously shown is plotted in figure 3.4b. We can see that all along the imaged regions of the crystal, the step density increases linearly with distance from the apex.

3.3 Discussion

To further understand what is happening close to the center, we tried to quantify the surface structure by looking at the ratio of defect sites on the surface. From the STM images, we notice a good overlap of terrace widths throughout the curvature with the exception of ∼ 40 μm around the center. We also notice that there is a strong presence of step bunching and vacancy islands near the apex occurring within the 100-200 μm about the center. Throughout the rest of the curvature the step edges mostly are straight with not much step bunching with the exception of regions which might have macroscopic scratches at the surfaces. At the edges of the crystal, the step edges are almost all parallel linear and equidistant. We believe that the increased defects around the apex is a result of the crystal not reaching thermodynamic equilibrium at larger terraces for the current annealing temperature. To verify this, we would expect an increase in number of defect sites around the center.

We do so by taking a ratio of the number of edge atoms to the number of terrace atoms, d_{tot}, normalized by what ratio is expected, d_{exp}, at that step density, $\frac{d_{tot}}{d_{exp}}$. Where the crystal only has edge atoms from the terrace widths for the expected terrace width, we expect a value of 1. Where there is an excess in edge atoms due to step bunching or vacancy islands, we expect a value larger than 1. Figure 3.5 shows these ratios for the up to 250 μm from the apex. Beyond 100 μm from the apex, the ratio is estimated from the average terrace widths per image assuming the terraces are per-

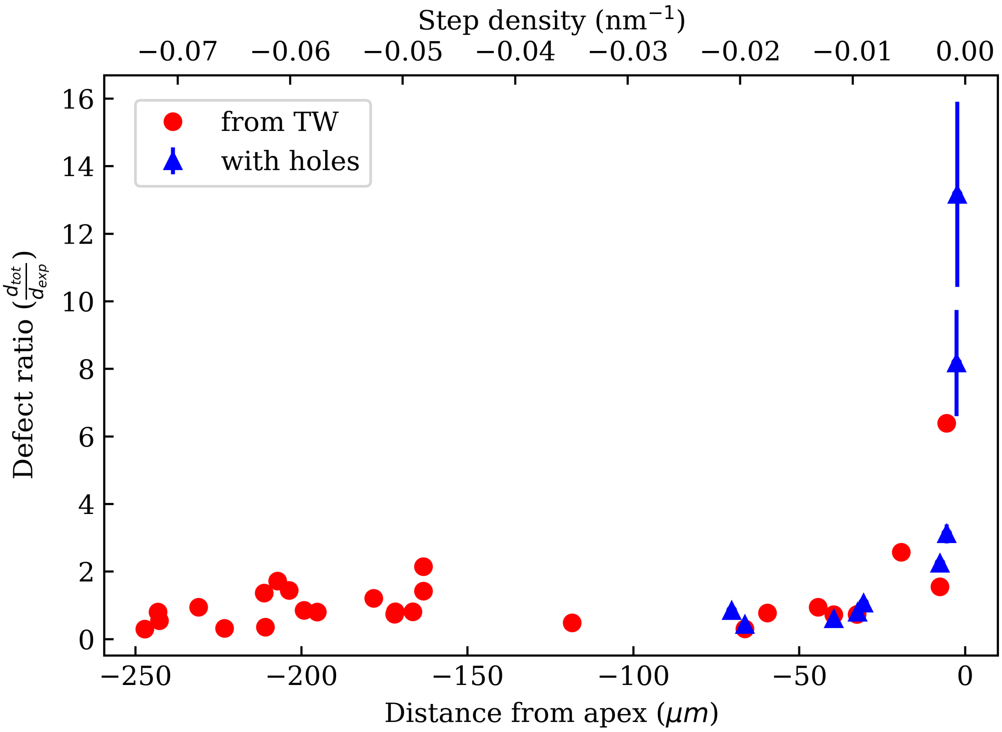

Figure 3.5: *Defect ratio as a function of distance from the apex (or expected step density on top axis). Red circles represent surfaces with no vacancy islands. Blue triangles represent images with vacancy islands.*

fectly parallel and straight. These ratios all fluctuate around 1, with perhaps a slight increase approaching the center as the approximation worsens. Within 100 μm from the apex, the number of step atoms is accurately measured tracing the steps in each image in a image analysis software [9]. Red circles indicate images with no vacancy islands. Blue triangles represent images where there were vacancy islands. Beyond 100 μm, where we have proper surface reconstruction, the values are spread around 1. Between 100 and 20 μm, where we expect the value to start increasing, the ratio of reactive sites is still near thermodynamic equilibrium despite the starting to have noticeable surface defects. Within the 50 μm around the apex, we observe a steep increase in defect sites. From these results, we can conclude that the number of step atoms at a step density below 0.005 nm^{-1}, or expected terrace width of more than 200 nm, does not match that of what we would expect for annealing temperatures of 920 C. For experiments on surface reactivity, this would explain any discrepancies which occur at such step densities.

Version of March 31, 2020– Created March 31, 2020 - 09:26

Chapter 4

Conclusion

This thesis presents the characterization of a curved platinum crystal exhibiting chiral kinked step edges. Auger electron spectroscopy demonstrates that cleaning of our platinum crystal was successful. Low energy electron spectroscopy has shown that the surface structures very nicely agrees with the literature. STM results show that the step density increases linearly as a function of the distance from the apex. However, below 0.005 nm^{-1}, where terrace widths are expected to be larger than 200 nm, we are no longer in thermodynamic equilibrium and experience an surplus in reactive sites.

Further research can be done on limonene adsorption. It would be interesting to observe the chiral surfaces while doing temperature programmed desorption under only (R) enantiomer, only (S) enantiomer or a mixture. This could lead to new fields of research including using chiral surfaces to sort chiral molecules.

Bibliography

[1] M. Corso, F. Schiller, L. Fernández, J. Cordón, and J. E. Ortega, *Electronic states in faceted Au(111) studied with curved crystal surfaces*, Journal of Physics: Condensed Matter **21**, 353001 (2009).

[2] R. van Lent, S. V. Auras, K. Cao, A. J. Walsh, M. A. Gleeson, and L. B. F. Juurlink, *Site-specific reactivity of molecules with surface defectsâThe case of H2 dissociation on Pt*, Science **363**, 155 (2019).

[3] K. Cao, R. van Lent, A. W. Kleyn, M. Kurahashi, and L. B. F. Juurlink, *Steps on Pt stereodynamically filter sticking of O2,* Proceedings of the National Academy of Sciences **116**, 13862 (2019).

[4] D. S. Sholl, *Adsorption of chiral hydrocarbons on chiral platinum surfaces*, Langmuir **14**, 862 (1998).

[5] C. F. Mcfadden, P. S. Cremer, and A. J. Gellman, *Adsorption of Chiral Alcohols on "Chiral" Metal Surfaces*, Technical report.

[6] M. A. Van Hove and G. A. Somorjai, *A new microfacet notation for high-Miller-index surfaces of cubic materials with terrace, step and kink structures*, Surface Science **92**, 489 (1980).

[7] T. Michely and G. Comsa, *Temperature dependence of the sputtering morphology of Pt(111)*, Technical report, 1991.

[8] A. M. Lahee, J. R. Manson, J. P. Toennies, and C. Wöll, *Observation of Interference Oscillations in Helium Scattering from Single Surface Defects*, Phys. Rev. Lett. **57**, 471 (1986).

[9] D. Nečas and P. Klapetek, *Gwyddion: an open-source software for {SPM} data analysis*, Central European Journal of Physics **10**, 181 (2012).